A simulation study of the role of anisotropic charge transport and grain boundary recombination in thin-film Sb_2Se_3 photovoltaics

R.A. Lomas-Zapata [*], A.W. Prior, B.G. Mendis [*]

Dept. of Physics, Durham University, South Road, Durham DH1 3LE, UK

ABSTRACT

The crystal structure of Sb_2Se_3, which consists of [0 0 1] oriented ribbons held together by weak van der Waals forces, gives rise to unique absorber layer properties different from other more conventional photovoltaic materials, such as Si or CdTe. Charge carrier transport occurs preferentially along the ribbon direction, and grain boundary recombination is minimal provided the ribbons are oriented parallel to the grain boundary plane. For optimum performance the Sb_2Se_3 absorber layer must have a (0 0 1) orientation, although in practice (2 1 1) and (2 2 1) growth textures are more common. The effect of this non-ideal orientation on anisotropic charge carrier transport and grain boundary recombination has however not been quantified. Here we derive analytical expressions for charge transport along a 1D ribbon under different boundary conditions. The local device properties for a given microstructural feature (e.g. grain boundary) can then be simulated by superposition of all individual ribbon contributions. It is found that anisotropic charge transport has the largest impact on device properties, even in the presence of electrically active grain boundaries (10^7 cm/s recombination velocity). For example, a $44°$ ribbon misorientation (i.e. (2 2 1) growth texture) resulted in a ~3% efficiency loss compared to the ideal (0 0 1) orientation. This highlights the importance of ribbon misorientation for achieving the highest efficiency Sb_2Se_3 devices.

1. Introduction

Sb_2Se_3 is a promising material for thin-film solar cells due to its abundance, non-toxicity, and ideal optical and electronic properties, such as high absorption coefficient (10^5 cm^{-1}) and bandgap (1.1 eV) [1]. Sb_2Se_3 is highly anisotropic due to its ribbon-like structure, which consists of Sb_4Se_6 structural units linked by covalent bonds along the *c*-axis, and weakly bound to its neighbouring ribbons by van der Waals interactions along the *ab*-plane ([2]; here we adopt the *Pbnm* space group classification). Sb_2Se_3 therefore has the potential to mitigate the effect of dangling bonds at grain boundaries, so long as the grain boundary plane is oriented parallel to the ribbons [3]. This is because for such a grain boundary the ribbons remain intact, with only the weak van der Waals bonding being disrupted. Therefore, at most only shallow defect states will be introduced at the grain boundary. However, density functional theory (DFT) studies have indicated that Sb_2Se_3 grain boundary planes that are non-parallel to the ribbon direction can potentially be passivated by undergoing structural relaxation [4], which causes the deep defect states to be removed, thus reducing the Shockley-Read-Hall recombination rate.

The hole mobilities along the *a*, *b*, and *c*-directions are reported to be 1.17, 0.69, and 2.59 cm^2 V^{-1} s^{-1} respectively [5]. Carrier transport along the ribbon *c*-direction is therefore the most efficient. This is also supported by Boltzmann transport simulations, where the highest electron mobility (the parameter of interest for p-type Sb_2Se_3 absorber layers) was found to be along the ribbon direction with an extremely large anisotropy ratio of 46 [6]. However, for electron transport along the *ab*-plane to occur, electrons must be transferred between neighbouring ribbons by hopping across the van der Waals gap. Due to the lower mobilities associated with charge carrier transport along the *a*- and *b*-directions, transport along either direction is undesirable. By reducing the inter-ribbon hopping and promoting transport along the high mobility *c*-direction, the efficiency of Sb_2Se_3 devices can be improved. This requires the growth orientation of Sb_2Se_3 grains to be carefully controlled. However, experimental data suggests that (0 0 1) may not be the preferred growth orientation [7], and instead (2 1 1) and (2 2 1) are the most commonly found grain textures [8,9], although depending on the deposition method orientations such as (1 2 0) and

---
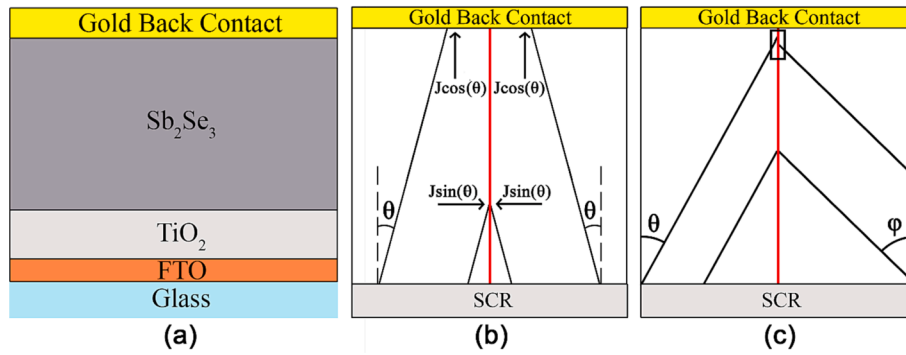
Fig. 1. (a) Schematic of device architecture used in the simulations. (b) Single, symmetric grain boundary with misorientation angle θ. The long ribbon is under the space charge region (SCR) to back contact (BC) transport scenario, while the short one is under the SCR to grain boundary (GB) transport scenario. The arrows depict the incident current density contributing to recombination at their respective recombination surface. (c) Asymmetric grain boundary, where the ribbon misorientation angles are θ and φ, respectively. Due to the geometry, bundling may be required to match the end positions of the ribbons along the grain boundary (see text for further details). The top right ribbon does not reach the SCR, and therefore does not contribute to the device current.

(0 2 0) can also occur [10]. The highest cell efficiency records for Sb$_2$Se$_3$, i.e. 9.2% [11] and 10.1% [12], both consist of (0 0 1) oriented ribbons, indicating the importance of orientation for the device efficiency. By comparison the record cell efficiencies for more established thin-film photovoltaics, such as CdTe, Cu(In,Ga)S$_2$ and hybrid perovskites are all above 20% [13]. The lower values for Sb$_2$Se$_3$ could be due to the technology being in the relatively early stages of development, since the spectroscopic limited maximum efficiency for the material is calculated to be 28.2% [14].

Since current polycrystalline thin-films of Sb$_2$Se$_3$ are far from the ideal growth condition, the exact role of misorientation on device efficiency must be quantified. In particular, the misorientation will affect the anisotropic charge transport, as well as any grain boundary recombination. Thin-film solar cells have complex microstructures and modelling the device properties can therefore be quite challenging. For example, recent 3D device simulations using the Synopsys Sentaurus TCAD finite element software [15] for CdTe and Cu$_2$ZnSnSe$_4$ thin-film solar cells only included two and five grains respectively [16,17]. However, for Sb$_2$Se$_3$ a simplification can be made, which assumes the carrier transport is predominantly along the ribbon direction, with inter-ribbon hopping being negligible. This reduces carrier transport to a 1D problem, which can be solved analytically. In this work, we derive the analytical solutions for ribbon transport under the different scenarios found in polycrystalline thin-film Sb$_2$Se$_3$. These equations can then be used to simulate complex device microstructures in a computationally efficient manner. Previous simulation work on Sb$_2$Se$_3$ has focussed on optimising the device architecture, such as the introduction of a back surface field [18], addition of hole transport layers [19–20], relative merits of Sb$_2$Se$_3$ vs. Sb$_2$S$_3$ absorber layers [21] and pn-homojunction Sb$_2$Se$_3$ absorber layers [22]. To our knowledge, this is the first investigation into the role of anisotropic charge transport and grain boundaries (symmetric and asymmetric) on Sb$_2$Se$_3$ device efficiency. Our results provide an insight into the dominant contributing factors currently limiting the efficiency of Sb$_2$Se$_3$ thin-film solar cells.

2. Simulation method

The Sb$_2$Se$_3$ thin-film device architecture is based on experiment [14], and is illustrated schematically in Fig. 1a. It consists of fluorine doped tin oxide (FTO; 500 nm layer thickness), n-layer TiO$_2$ (50 nm), p-absorber layer Sb$_2$Se$_3$ (3000 nm) and gold back contact deposited on a glass superstrate. In this work we perform 2D device simulations, which may or may not include a grain boundary. As an example, Fig. 1b shows a device with only a single symmetric grain boundary, where the ribbons are mirror reflected across the grain boundary plane and have constant misorientation angle θ with respect to the film thickness direction. For

an asymmetric grain boundary however, the ribbon misorientation either side of the grain boundary plane will be different (Fig. 1c). The simulations assume columnar Sb$_2$Se$_3$ grains with a grain 'diameter' of 1000 nm, consistent with experiment [14].

The carrier transport along each ribbon is calculated separately, assuming negligible inter-ribbon hopping, and the contributions from all the ribbons within the simulation 'volume' summed to give a current density (*J*)-voltage (*V*) curve. It should be emphasised that for a grain boundary what is calculated is the local *JV* response. An actual device will contain many Sb$_2$Se$_3$ grains, and therefore the measured *JV* curve is a global average of individual grain boundaries of varying misorientation. Carrier transport along a given ribbon can be classified according to the boundary conditions. Four charge transport scenarios are identified, namely space charge region (SCR) to back contact (BC), SCR to grain boundary (GB), grain boundary to back contact, and grain boundary to grain boundary (exclusively present at high misorientation angles). However, only the ribbon transport from space charge region to both the back contact and grain boundary will contribute to the device current density (Fig. 1b). In the next section analytical equations for the two important transport scenarios are presented.

2.1. Analytical equations

2.1.1. Continuity equation

Charge transport in a semiconductor is described by the continuity equations [23,24]. Under steady-state conditions this reduces to Equation (1) for minority carrier electrons in a p-type semiconductor such as Sb$_2$Se$_3$:

$$D_n \frac{d^2 n}{dx^2} + \mu_n \frac{d(nE)}{dx} + G - \frac{(n - n_0)}{\tau} = 0 \tag{1}$$

where D_n and μ_n are the electron diffusion coefficient and mobility, n is the electron concentration which has equilibrium value n_0, E is the electric field, and τ is the overall carrier lifetime, which includes radiative and non-radiative recombination. The generation rate G for photons of energy $h\nu$ is given by:

$$G(h\nu, x) = N_{ph}(h\nu)\alpha(h\nu)e^{-\alpha(h\nu)x} \tag{2}$$

where $N_{ph}(h\nu)$ is the number of photons incident in the Sb$_2$Se$_3$ layer after correcting for absorption and reflection at the different layers and interfaces in a solar cell device, $\alpha(h\nu)$ is the absorption coefficient and x is the position along the film thickness direction. In the quasi-neutral region the electric field is negligible, and Equation (1) is reduced to what is commonly known as the minority-carrier diffusion equation:

$$D_n \frac{d^2(\Delta n)}{dx^2} - \frac{\Delta n}{\tau} = -G(h\nu, x) \tag{3}$$

This differential equation is solved for the excess electron concentration, $\Delta n = n - n_0$, by calculating the complementary function and particular integral [25]. The excess carrier concentration is:

$$\Delta n(h\nu, x) = C_1 e^{\frac{x}{L_n}} + C_2 e^{\frac{-x}{L_n}} - \frac{N_{ph} L_n^2 \alpha e^{-\alpha x}}{D_n(\alpha^2 L_n^2 - 1)} \tag{4}$$

where $L_n = \sqrt{D_n \tau}$ is the diffusion length. The coefficients C_1 and C_2 are calculated using the boundary conditions corresponding to each transport regime. Due to the nature of this study, it is more convenient to express Equation (4) along the ribbon thickness direction (r), rather than the film thickness direction (x). For a ribbon misorientation angle θ this gives:

$$\Delta n(h\nu, r) = C_1 e^{\frac{r}{L_n}} + C_2 e^{\frac{-r}{L_n}} - \frac{N_{ph} L_n^2 \alpha e^{-\alpha r \cos(\theta)}}{D_n(\alpha^2 L_n^2 - 1)} \tag{5}$$

2.1.2. Boundary conditions

The boundary conditions for a ribbon extending from the space charge region to back contact are given by the following equations:

$$\Delta n(r) = \frac{n_i^2}{N_A} \left[e^{\left(\frac{qV}{kT}\right)} - 1 \right] \tag{6a}$$

$$D_n \frac{d\Delta n(r)}{dr} \cos(\theta) = -S_{BC}[\Delta n(r)] \tag{6b}$$

where S_{BC} is the recombination velocity at the back contact surface, n_i and N_A are the intrinsic carrier and acceptor concentrations respectively, q is the magnitude of the electron charge, V is the applied bias of the device and kT is the thermal energy. A $\cos(\theta)$ term is present for recombination at the back surface, since only the current density component normal to the back contact must be considered (Fig. 1b). Using these boundary conditions the coefficients C_1 and C_2 in Equation (5) can be solved for a SCR-BC ribbon.

Next, consider ribbons that extend from the space charge region to a grain boundary. The boundary condition at the space charge edge is identical to Equation (6a). However, the boundary condition at the grain boundary depends on the simulation case. For a symmetric grain boundary we have:

$$2D_n \frac{d\Delta n(r)}{dr} \sin(\theta) = -S_{GB}[\Delta n(r)] \tag{7}$$

The $\sin(\theta)$ factor arises since we only consider the current density component normal to the grain boundary plane. Furthermore, due to symmetry, ribbons on both side of the grain boundary contribute equal current densities, which explains the factor of 2 in Equation (7); see also Fig. 1b. The C_1 and C_2 coefficients for a SCR-GB ribbon in the symmetric grain boundary case can therefore be solved using Equations (6a) and (7).

Consider now an asymmetric grain boundary. Since only the ribbons extending to the space charge region edge contribute to the current density of the device, two sets of boundary conditions are obtained for an asymmetric grain boundary, which are referred to as 'paired' and 'unpaired' boundary conditions. The 'paired' case consists of ribbons for both grains extending from the space charge region edge to the grain boundary plane, while for the 'unpaired' case this condition is only satisfied for ribbons in one of the grains (Fig. 1c). For an asymmetric grain boundary the C_1 and C_2 coefficients will be different for ribbons in each grain, and therefore a total of four boundary conditions are required.

For the 'paired' case the boundary condition at the space charge region edge (Equation (6a)) is valid for both grains, and provides two of the four boundary conditions. The third boundary condition at the grain

boundary plane is similar to Equation (7), but with modifications due to the reduced symmetry:

$$R_1 D_n \frac{d\Delta n(r_{LHS})}{dr} \sin\theta + R_2 D_n \frac{d\Delta n(r_{RHS})}{dr} \sin\varphi = -\frac{S_{GB}}{2} [\Delta n(r_{LHS}) + \Delta n(r_{RHS})] \tag{8}$$

The subscripts 'LHS' and 'RHS' refer to the left and right hand sides of the grain boundary. In general, two ribbons may not meet at exactly the same grain boundary position (Fig. 1c), so that the microscopic current density flux normal to the grain boundary plane may only be due to one grain. This can be accounted for by 'bundling' the ribbons, i.e. we consider a finite grain boundary segment, which consists of multiple ribbons. The grain boundary segment must be sufficiently large to smooth out any microscopic variations, while at the same time being sufficiently small to accurately model carrier transport at the continuum level. R_1 and R_2 in Equation (8) are then the relative number fraction of ribbons on the left and right grains (misorientation angles θ and φ respectively). They can be calculated by geometry and have values within the range [0,1]. The grain with the largest misorientation angle (and therefore the highest number of ribbons per bundle) has an R-value equal to one, so that the R-value for the second grain is ≤ 1. Defining R-values in this manner ensures that equation (8) is consistent with equation (7) for a symmetric grain boundary, since for $\theta = \varphi$ we have $R_1 = R_2 = 1$. The fourth boundary condition is given by:

$$\Delta n(r_{LHS}) = \Delta n(r_{RHS}) \tag{9}$$

Equation (9) is obtained by noting that continuity requires the excess carrier concentration (Equation (5)) for the ribbons on the left hand side (r_{LHS}) and right hand side (r_{RHS}) to be equal at the grain boundary plane.

For the 'unpaired' case, since only the ribbons from one of the grains extend to the space charge region edge, a new boundary condition must be included in order to solve the system of equations:

$$R_1 D_n \frac{d\Delta n(r_{LHS})}{dr} \cos\theta = R_2 D_n \frac{d\Delta n(r_{RHS})}{dr} \cos\varphi \tag{10}$$

This boundary condition is due to the fact that the minority carrier concentration is continuous across the grain boundary plane (Equation (9)), and therefore the diffusion current density parallel to the boundary plane must also be continuous. Equations 8–10 along with Equation (6a) for the ribbon extending to the space charge edge are therefore the four boundary conditions for the 'unpaired' case. It can be shown that the current densities for an asymmetric grain boundary ('paired' and 'unpaired' boundary conditions) reduce to the simpler form for a symmetric grain boundary when $\theta = \varphi$. Analytical solutions for all transport scenarios are given in the Supplementary Information.

2.1.3. Current density

The diffusion current density for electrons is given by [24]:

$$J_{Diff} = qD_n \frac{d\Delta n(r)}{dx} \tag{11}$$

The concentration gradient $\frac{d\Delta n}{dx}$ is evaluated at the space charge edge. Expressions for $\Delta n(r)$ depend on the transport scenario and hence boundary conditions. The diffusion current density consists of two contributions, the dark current density, and the quasi-neutral current density. The former is the current density due to the applied bias, while the latter is the photo-generated current density due to carrier diffusion within the quasi-neutral region. The dark and quasi-neutral current densities flow in opposite directions to one another. Analytical expressions for the diffusion, dark and quasi-neutral current densities in the SCR-BC and SCR-GB transport scenarios are given in the Supplementary Information.

The space charge region current density due to drift of electrons photo-generated within the space charge region is given by:

$$J_{SCR} = qN_{ph}\left[1 - e^{-\alpha X_p}\right] \tag{12}$$

Table 1

Material properties and simulation parameters. 'CB' and 'VB' denote conduction and valence bands respectively. Where applicable, references for materials parameters are indicated.

Material properties	Sb$_2$Se$_3$	TiO$_2$
Thickness (nm)	3000 [29]	50 [29]
Grain width (nm)	1000 [29]	–
Bandgap (eV)	1.17 [5]	3.2 [30]
Electron affinity (eV)	4.04 [31]	4.20 [32]
Dielectric constant	18 [5]	10 [32]
CB effective density of states (cm^{-3})	2.2×10^{18} [33]	2.2×10^{18} [34]
VB effective density of states (cm^{-3})	1.8×10^{19} [31]	6.0×10^{17} [35]
Electron mobility (cm^2 V^{-1}s^{-1})	16.9 [5]	20 [36]
Acceptor doping N$_A$ (cm^{-3})	10^{16} [37]	–
Donor doping N$_D$ (cm^{-3})	–	10^{17} [35]
Carrier lifetime (s)	10^{-9}	–
Temperature (K)	300	

where X_p is the space charge region width. It is assumed that the electric field is sufficiently strong to enable complete collection of all electrons photo-generated within the space charge region. The total current density for a given ribbon is the sum of Equations (11) and (12).

2.2. Simulation parameters and methodology

The incident light used is Air Mass 1.5 global tilt [26] normalised to 1 sun (1000 W/m^2). Absorption and reflection of the light as it passes through the different layers of the device (Fig. 1a) is modelled using the complex dielectric function for the given material ([27] for FTO, [28] for TiO$_2$ and experimental data for Sb$_2$Se$_3$, kindly provided by Dr Jon Major, University of Liverpool). Normal incidence of the light is assumed, and multiple reflection at the layer interfaces is not taken into account. The simulation runs for an applied bias voltage of −0.10 to 1.20 V, in steps of 0.01 V. The current density is calculated for each ribbon, at each bias voltage and incident light wavelengths in the range 300 to 900 nm. Further simulation parameters are listed in Table 1.

For a grain boundary simulation, the microstructure is non-uniform, and the diffusion current density for each ribbon will be a function of the ribbon end position along the grain boundary plane. The space charge

region current density is however uniform for all ribbons. The total diffusion current density can be calculated by summing the individual current contributions from each ribbon and dividing by the cross-sectional area (A) of the simulation supercell. In the Sb$_2$Se$_3$ crystal structure each ribbon has an 'area' of $ab/2$ perpendicular to the c-axis, where a and b are unit cell lattice parameters. The cross-sectional area for an inclined ribbon, projected along the plane of the device, is therefore $\frac{ab}{2\cos\theta}$. The current flowing along a given ribbon is equal to the current density multiplied by the (projected) ribbon cross-sectional area. The cross-sectional area A is given by $A = dw$, where d is the full width of the simulation supercell (i.e. twice the Sb$_2$Se$_3$ grain size) and w is the supercell depth. Here it is assumed that the depth direction is parallel to the a-axis of the Sb$_2$Se$_3$ unit cell, so that for a single ribbon w will be equal to the a lattice parameter. The exact choice of w is not critical, since the a and b lattice parameters for Sb$_2$Se$_3$ have similar values (i.e. 11.6 and 11.8 Å respectively [5]). The total current density is therefore:

$$J(V) = \int \left[J_{SCR}(V,\lambda) + \frac{ab}{2A\cos\theta} \sum_n J_{Diff,n}(V,\lambda) \right] \cos\theta d\lambda \tag{13}$$

where the summation is over all ribbons n and the integration is over all incident photon wavelengths λ. The diffusion current density for each individual ribbon, $J_{Diff,n}(V,\lambda)$, is calculated using Equation (11), while $J_{SCR}(V,\lambda)$ is given by Equation (12). The current densities are a function of bias, due to the fact that the space charge width also varies with applied voltage V. The $\cos\theta$ term accounts for the current density component collected by the device.

In order to reduce the computational time for grain boundary simulations, a bundling strategy, similar to that described for the asymmetric grain boundary (section 2.1.2), was implemented. Instead of solving each ribbon individually, they were grouped together and solved using the average end position along the film thickness direction of the bundle. The summation in Equation (13) is therefore over all bundles within the grain, rather than ribbons. Furthermore, the current densities must be multiplied by the number of ribbons within a given bundle.
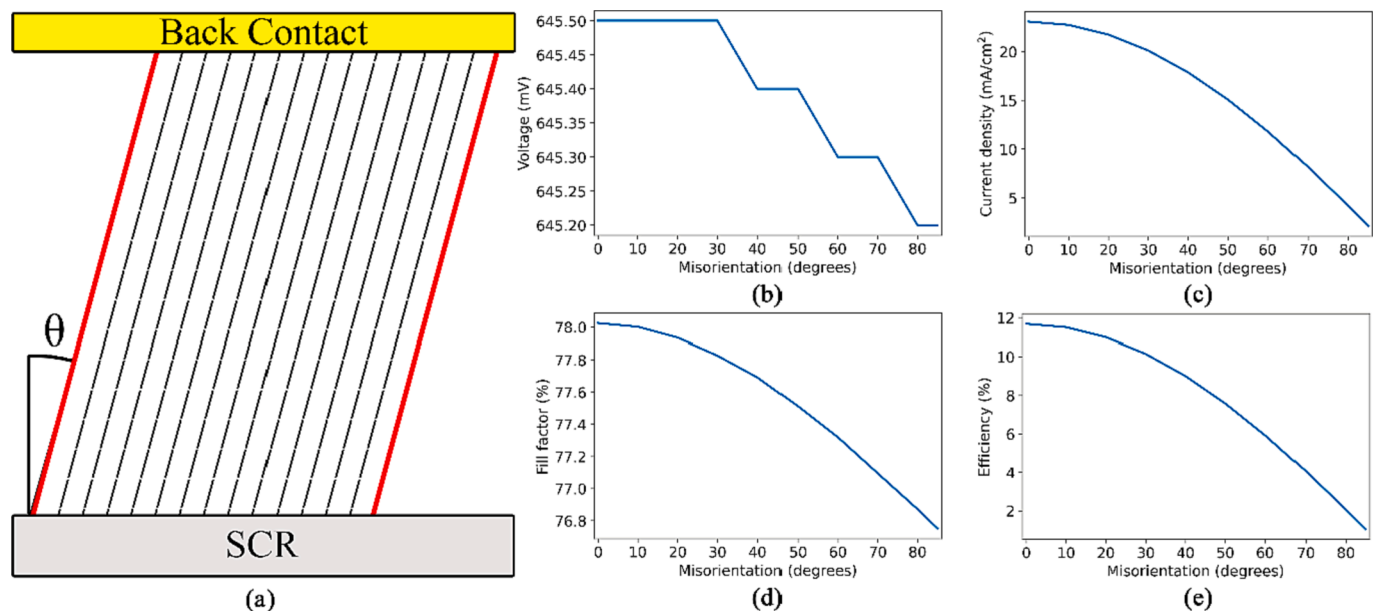
Fig. 2. (a) Single grain with ribbons misoriented by angle θ. The red lines indicate grain boundaries running parallel to the ribbons. (b) Open circuit voltage (V_{OC}), (c) short circuit current density (J_{SC}), (d) fill factor and (e) device efficiency as a function of ribbon misorientation. The step-like appearance of V_{OC} is due to discrete sampling of θ (10° intervals); the line is a guide to the eye. (For interpretation of the references to colour in this figure legend, the reader is referred to the web version of this article.)
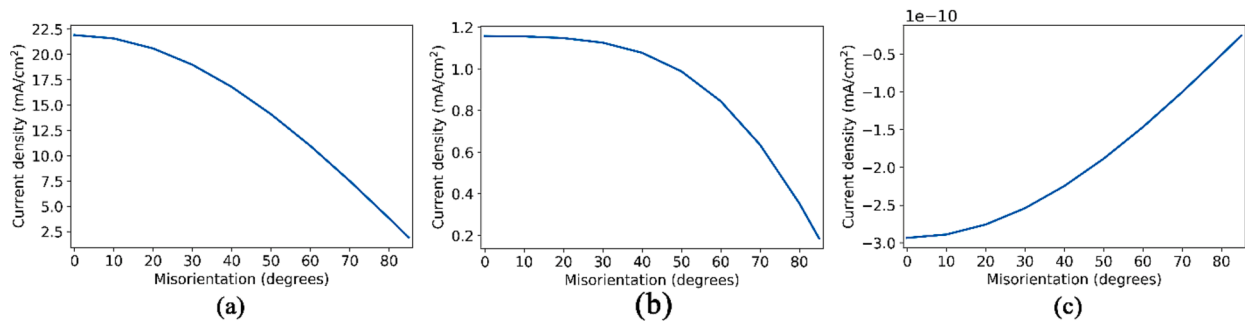
Fig. 3. (a) Space charge region current density (J_{SCR}), and (b) quasi-neutral region current density (J_{QNR}) at zero bias condition (V = 0). (c) Dark current density (J_{Dark}) at −1 V reverse bias, which is approximately equal to the diode reverse saturation current density. The current densities are plotted as a function of the ribbon misorientation angle. Note the change in current density scale in (c).

3. Results and discussion

3.1. Effect of anisotropic charge transport (single grain)

In this simulation only the effect of ribbon misorientation (θ) on the device efficiency is considered. The simulation consists of a single grain with c-axis tilted by an angle θ with respect to the film thickness direction, the ribbons extending from the pn-junction to the back contact. The grain boundary surface runs parallel to the ribbon orientation (Fig. 2a), and therefore has no effect on this grain. The device parameters as a function of ribbon misorientation are shown in Fig. 2b to 2e (see Supplementary Information for individual JV-curves).

The main factor determining the efficiency of the device is the short-circuit current density (J_{SC}). Photo-current density contributions at zero bias from space charge region (J_{SCR}), quasi-neutral region (J_{QNR}), as well as the −1 V reverse bias dark current density (J_{Dark}) are shown in Fig. 3. In this work the photo-current density is defined as being positive, while the dark current density is negative. The main contributor to J_{SC} is the space-charge region current density (Fig. 3a), which decreases

monotonically with misorientation angle, due to the $\cos\theta$ geometric factor for tilted ribbons (Equation (13)). At larger misorientation angles however, the contribution of the quasi-neutral region (Fig. 3b) becomes significant as J_{SCR} steadily decreases. J_{QNR} is nearly constant for misorientation angles below $\sim 30°$, but decreases rapidly beyond that. This is due to the competing effect of two factors. For a given absorber layer thickness the length of a ribbon increases with misorientation angle, so that the photo-generated carriers must diffuse along a longer segment of the ribbon to reach the back contact. This reduces the back contact recombination. However, the decrease in photo-current losses is opposed by the $\cos\theta$ geometric factor, which becomes dominant for $\theta > 30°$. The absolute value of the dark current density (Fig. 3c) has a similar shape as J_{SCR}, and can therefore be attributed to the $\cos\theta$ geometric factor. The absorber layer thickness (3000 nm) is much larger than the electron diffusion length (~ 209 nm), meaning that the change in ribbon length with misorientation has very little influence on excess charge carriers injected at the space charge edge during electrical biasing (Equation (6a)). In other words, the long diode approximation is valid for J_{Dark} along the ribbon direction.
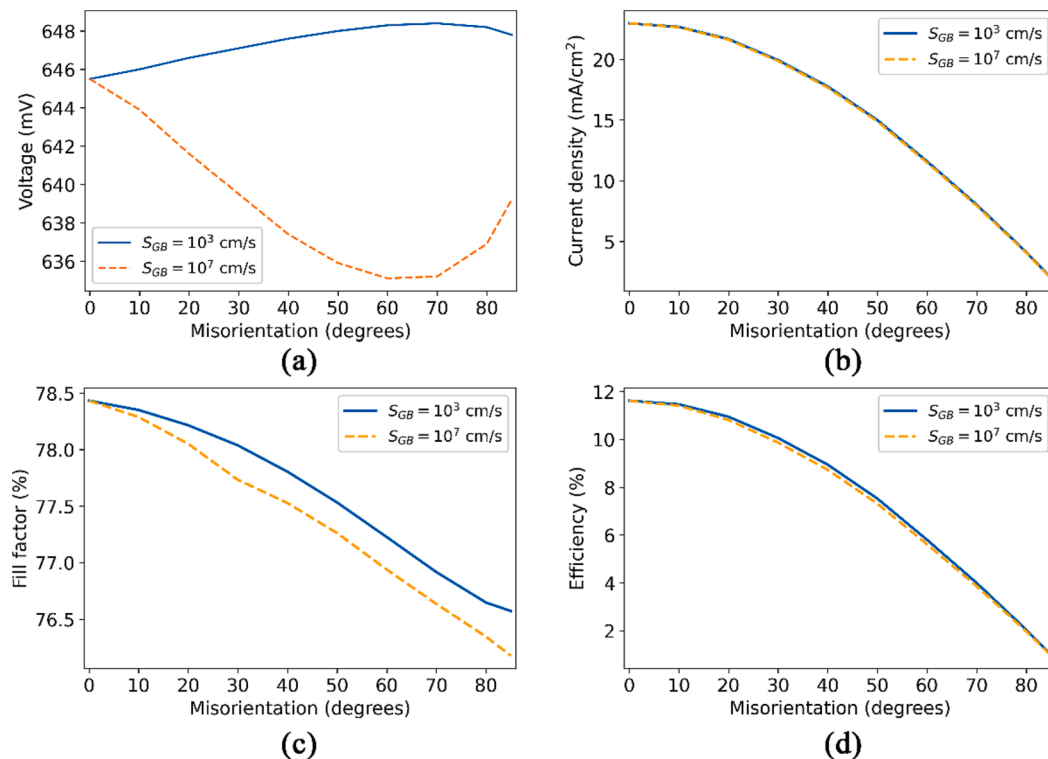
Fig. 4. Comparison between passivated and non-passivated symmetric grain boundaries. (a) Open circuit voltage (V_{OC}), (b) short circuit current density (J_{SC}), (c) fill factor, (d) device efficiency as a function of ribbon misorientation (θ). S_{GB} is the grain boundary recombination velocity.
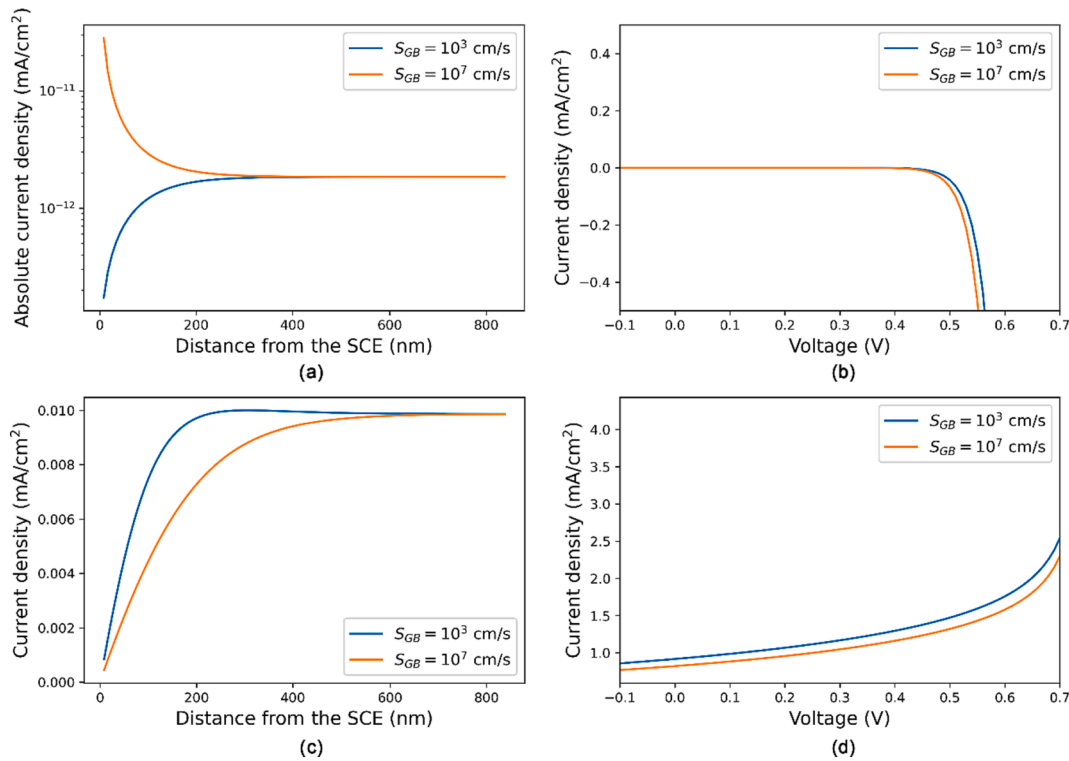
Fig. 5. (a) Dark current density at -1 V bias and $\theta = 50°$, plotted as a function of ribbon bundle end position along the grain boundary plane. The absolute value of the dark current density is displayed on a logarithmic scale, while the ribbon end position is measured as the vertical distance from the space charge edge (SCE). (b) Total dark current density for all ribbon bundles as a function of applied bias V. (c) Quasi-neutral region current density at $V = 0$, $\theta = 50°$, as a function of ribbon bundle end position along the grain boundary plane, measured as vertical distance from the SCE. (d) Total quasi-neutral current density for all ribbon bundles as a function of applied bias.

Although J_{SCR} is dominant at zero bias and largely governs J_{SC}, it decreases dramatically close to the open circuit voltage (V_{OC}) due to a shrinking space charge width. Under these conditions, J_{Dark} and J_{QNR} are important, and their combined effect can be observed as a slight decrease in V_{OC} and fill factor. The general downward trend of the efficiency suggests that in order to maximise device performance the ribbons must be oriented along the layer thickness direction (i.e. $\theta = 0°$). Most Sb$_2$Se$_3$ thin-films have a (2 1 1) or (2 2 1) growth texture [5], with ribbon misorientation angles of $37°$ and $44°$ respectively. For our simulation parameters a $44°$ ribbon misorientation results in a ~3 % efficiency loss compared to the ideal $0°$ microstructure. This highlights the importance of anisotropic charge transport on the overall device efficiency.

3.2. Grain boundary recombination

Here the effects of grain boundary recombination and anisotropic charge transport are analysed for two adjacent grains (Fig. 1b and 1c). Two cases are simulated, namely a passivated and non-passivated grain boundary. In the passivated grain boundary regime, the recombination velocity is set to 10^3 cm/s, while for the non-passivated case the grain boundary recombination velocity is 10^7 cm/s. The motivation for the passivated grain boundary is the possibility of removing deep defect states at the grain boundary plane through structural relaxation [4]. Results are first presented for a symmetric grain boundary, which is more straightforward to interpret, before moving onto asymmetric grain boundaries.

3.2.1. Symmetric grain boundary

A comparison between the passivated and non-passivated symmetric grain boundary device parameters as a function of ribbon misorientation (θ) is shown in Fig. 4 (see Supplementary Information for individual J-V

curves). We again emphasise that these are local device parameters, since the simulation supercell contained only one grain boundary.

Since the space charge region current density depends on the space charge width (Equation (12)) and not the grain boundary, it remains constant for both passivated and non-passivated grain boundaries, and is the main contributor to J_{SC} (Fig. 4b). However, the diffusion current density terms (i.e. J_{Dark} and J_{QNR}) are significantly impacted by grain boundary recombination velocity, which in turn impacts V_{OC} and fill factor. For $\theta > 30°$ all ribbons are under the space charge region to grain boundary transport regime, resulting in large differences in V_{OC} between the two grain boundaries (Fig. 4a). The trends in V_{OC} and fill factor can be explained by examining the functional forms of J_{Dark} and J_{QNR}, as described below.

J_{Dark} for the SCR-GB transport regime depends on two important factors, the vertical distance of the ribbon end point from the space charge region edge ($X_{a,n}$), as measured along the film thickness direction, and the recombination velocity at the grain boundary (S_{GB}). The expression for J_{Dark} is:

$$J_{Dark} = \frac{qD_n n_i^2 \left[e^{\frac{qV}{kT}} - 1 \right]}{L_n N_A} \left\{ \frac{\frac{S_{GB}L_n}{2D_n\sin\theta}\cosh\left(\frac{X_{a,n}}{L_n\cos\theta}\right) + \sinh\left(\frac{X_{a,n}}{L_n\cos\theta}\right)}{\frac{S_{GB}L_n}{2D_n\sin\theta}\sinh\left(\frac{X_{a,n}}{L_n\cos\theta}\right) + \cosh\left(\frac{X_{a,n}}{L_n\cos\theta}\right)} \right\} \tag{14}$$

At high recombination velocity (10^7 cm/s) and depending on the misorientation angle θ, the $\left(\frac{S_{GB}L_n}{2D_n\sin\theta}\right)$ term is greater than one, leading to the curly bracket expression approximating to a hyperbolic cotangent $\coth\left(\frac{X_{a,n}}{L_n\cos\theta}\right)$, while at low recombination velocity (10^3 cm/s) this term is less than one, and therefore the curly bracket changes to that of a hyperbolic tangent $\tanh\left(\frac{X_{a,n}}{L_n\cos\theta}\right)$. Both the hyperbolic cotangent and hyperbolic tangent converge to the same value if the argument $\left(\frac{X_{a,n}}{L_n\cos\theta}\right)$ is
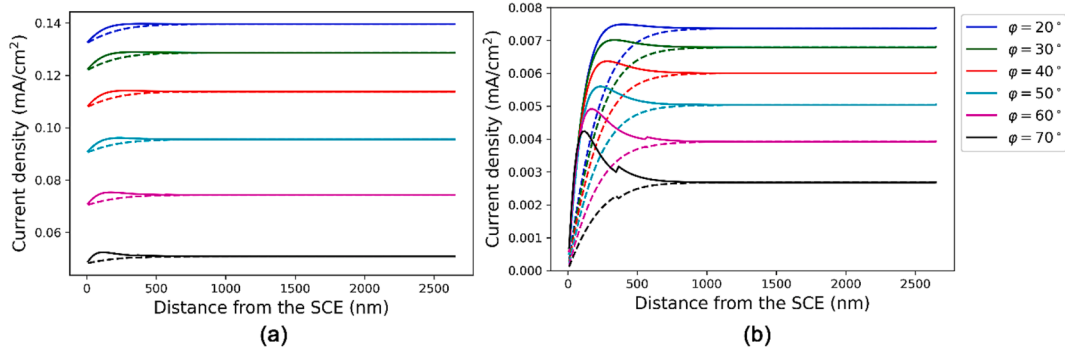
Fig. 6. (a) J_{SC} and (b) J_{QNR} (zero bias) for ribbon bundles as a function of end position along the grain boundary plane. The end position is measured as the vertical distance from the space charge edge (SCE). The ribbon misorientation θ is held fixed at 20°, while φ is varied between 20° – 70° in step sizes of 10°. Solid and dashed lines represent the passivated and non-passivated grain boundaries (10^3 and 10^7 cm/s recombination velocity) respectively.

greater than one. This effect can be clearly seen when comparing the dark current density for an individual ribbon bundle as a function of end position along the grain boundary plane (Fig. 5a). The total dark current density for all ribbons is shown in Fig. 5b.

The physical interpretation of this behaviour is as follows. The convergence of hyperbolic cotangent and tangent functions occur when the end point of an individual ribbon ($X_{a,n}$) is greater than the diffusion length component along the film thickness direction ($L_n\cos\theta$). In this scenario the dark current density is that of a long diode, and therefore independent of the grain boundary recombination velocity. For ribbon end points close to the space charge region edge, the dark current density is increased at high recombination velocities $\left(\frac{S_{GB}L_n}{2D_n\sin\theta} > 1\right)$, and reduced for low recombination velocities $\left(\frac{S_{GB}L_n}{2D_n\sin\theta} < 1\right)$. J_{Dark} has a component in the direction of the grain boundary, which means a higher dark current density is required to replenish the carriers lost to recombination in an electrically more active grain boundary. At high misorientation angles most ribbons terminate closer to the space charge region edge, and therefore the discrepancy between the passivated and non-passivated cases increases.

Similar considerations apply for the quasi-neutral region current density J_{QNR}, which contains equivalent terms in its analytical solution:

$$J_{QNR} = \frac{qN_{ph}L_n\alpha e^{-\alpha X_p}}{\left(L_n^2\alpha^2 - 1\right)}\left(F_{n1} - F_{n2}e^{-\alpha X_a}\right)$$

$$F_{n1} = \alpha L_n\cos\theta - \left\{\frac{\frac{S_{GB}L_n}{2D_n\sin\theta}\cosh\left(\frac{X_a}{L_n\cos\theta}\right) + \sinh\left(\frac{X_a}{L_n\cos\theta}\right)}{\frac{S_{GB}L_n}{2D_n\sin\theta}\sinh\left(\frac{X_a}{L_n\cos\theta}\right) + \cosh\left(\frac{X_a}{L_n\cos\theta}\right)}\right\}$$

$$F_{n2} = \frac{\alpha L_n\cos\theta - \frac{S_{GB}L_n}{2D_n\sin\theta}}{\frac{S_{GB}L_n}{2D_n\sin\theta}\sinh\left(\frac{X_a}{L_n\cos\theta}\right) + \cosh\left(\frac{X_a}{L_n\cos\theta}\right)} \tag{15}$$

J_{QNR} for an individual ribbon bundle as a function of end position along the grain boundary plane is shown in Fig. 5c. A clear difference between passivated and non-passivated grain boundary regimes is observed for ribbons terminating close to the space charge region edge, with ribbons under the passivated regime contributing up to 30% more current than those under the non-passivated regime. Fig. 5d shows the total J_{QNR} for all ribbons. As can be seen from Fig. 5b and 5d, close to V_{OC} the magnitude of J_{Dark} increases more rapidly compared to J_{QNR}. Furthermore, the onset of rapid increase in J_{Dark} (absolute value) occurs at a smaller bias for larger S_{GB} (Fig. 5c). This explains the lower V_{OC} and fill factor for the non-passivated grain boundary, compared to passivated grain boundaries (Fig. 4a and 4c). Despite the changes in V_{OC} and fill factor, the short circuit current density has the largest effect on overall efficiency, which is clear from the similar shape of the J_{SC}

(Fig. 4b) and efficiency (Fig. 4d) graphs. In particular, the misorientation dependence is dominated by the $\cos\theta$ geometric factor, indicating that anisotropic charge transport is more important than grain boundary recombination.

3.2.2. Asymmetric grain boundary

In a real device the absorber layer consists of grain boundaries with variable character, of which the symmetric grain boundary discussed in the previous section is a special case. It is therefore useful to analyse how deviations from a symmetric grain boundary would affect the local device properties. For this simulation the ribbon misorientation angles (θ, φ) across an asymmetric grain boundary were varied independently between 20° and 70°, for low and high grain boundary recombination velocities (i.e. 10^3 and 10^7 cm/s respectively), in order to analyse local device behaviour in more complex systems.

For asymmetric grain boundaries, depending on the misorientation angles, there can be up to three different transport regimes, namely space charge region to back contact, 'paired' and 'unpaired' space charge region to grain boundary ribbons. For most misorientation angles, one of the grains will have both 'paired' and 'unpaired' transport regimes, while the remaining grain will have only 'paired' transport. The grain with the smaller misorientation angle will have the 'unpaired' ribbons (see Fig. 1c). The effect this ribbon 'unpairing' has on the photocurrent density will now be described.

Fig. 6a is the short circuit current density for individual ribbon bundles as a function of end position along the grain boundary plane. One of the ribbon misorientation angles (θ) is kept fixed at 20°, while the other (φ) is varied between 20° − 70°. Results for both passivated and non-passivated grain boundaries are presented. As with other simulations, J_{SC} is dominated by J_{SCR}, although ribbons terminating between 100 and 600 nm from the space charge edge have higher J_{SC} for the passivated grain boundary. This difference between grain boundaries is due to the quasi-neutral current density, which is shown in Fig. 6b at zero applied bias for individual ribbon bundles as a function of end position. J_{QNR} is independent of grain boundary recombination velocity for ribbon end points larger than ∼ 600 nm from the space charge edge. This is due to the long diode behaviour discussed previously with Fig. 5a. The transition from 'paired' to 'unpaired' transport regimes is seen as a small spike in Fig. 6b, especially at large misorientation angles (>60°). It is clear that ribbon 'unpairing' is a relatively minor effect for our simulation geometry (i.e. grain size and absorber layer thickness), that is only observed when one of the ribbon misorientations is larger than 60°, and even then the net effect on J_{SC} is negligible.

The local device parameters for passivated and non-passivated asymmetric grain boundaries are shown in Fig. 7 (see Supplementary Information for representative J-V curves). In these two-dimensional plots V_{OC}, J_{SC}, fill factor and efficiency are mapped as a function of ribbon misorientation angles θ and φ. The diagonal (i.e. $\theta = \varphi$)
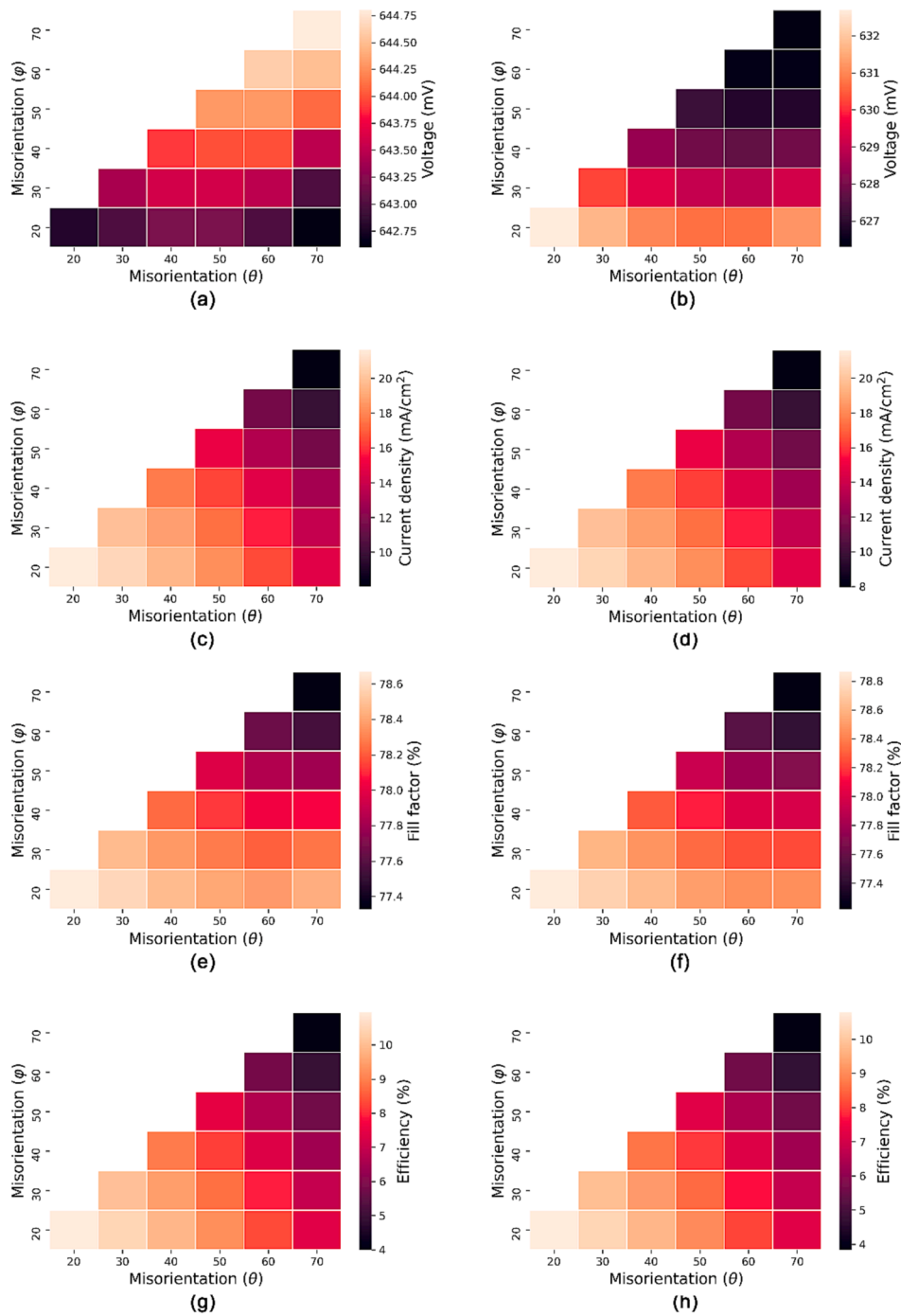
Fig. 7. Local device parameters for passivated (10^3 cm/s; left column) and non-passivated (10^7 cm/s; right column) asymmetric grain boundaries, plotted as a function of the ribbon misorientation angles θ and φ (expressed in degrees). Open circuit voltage (V_{OC}), short circuit current density (J_{SC}), fill factor and efficiency for the passivated grain boundary are shown in (a), (c), (e) and (g) respectively. The corresponding figures for the non-passivated grain boundary are (b), (d), (f) and (h).

corresponds to a symmetric grain boundary. The device properties have mirror symmetry across the diagonal, and therefore only one half of the figure is displayed for visual clarity. Similar to the symmetric grain boundary case, there is generally an increase in V_{OC} for the passivated grain boundary as either θ or φ, or both, is increased, while the opposite is true for the non-passivated grain boundary (Fig. 7a and 7b). Despite the clear difference in J_{QNR} for the passivated and non-passivated grain boundaries (Fig. 6b), the J_{SC} is dominated by J_{SCR}, which has a $\cos\theta$ (or $\cos\varphi$) geometric dependence. The J_{SC} plots are therefore very similar for the two grain boundaries (Fig. 7c and 7d). The fill factor for the non-passivated grain boundary is slightly higher than the passivated grain

boundary (Fig. 7e and 7f), due to the increased J_{Dark} contribution, particularly close to V_{oc} (see discussion in section 3.2.1). Finally, due to the overwhelming importance of J_{SCR}, the efficiencies for the two grain boundaries are almost equal. Therefore, the general trends observed for the symmetric grain boundary hold true for asymmetric grain boundaries as well.

4. Conclusions

Simulations indicate that, due to a relatively small diffusion length (~209 nm) for a typical carrier lifetime of 1 ns, only the charge carriers

generated within and close to the space charge region are collected, regardless of ribbon misorientation. Consequently, the misorientation of ribbons away from the ideal [001] direction has a bigger impact on the device efficiency than recombination at either the back contact or any grain boundary. For example, a 44° ribbon misorientation, corresponding to a (221) thin-film growth texture, results in 3.2% efficiency loss compared to the ideal ribbon orientation. On the other hand, passivating the back contact recombination velocity to 10^3 cm/s for the same ribbon misorientation had no effect on the efficiency within the accuracy of the simulation, while the introduction of a 44° symmetric grain boundary (10^7 cm/s recombination velocity) in the absorber layer with non-passivated back contact decreased the efficiency by only 0.2%. As discussed in Section 3.1 the largest changes in device efficiency with ribbon misorientation angle is due to the short circuit current density, which is dominated by the space charge region contribution (J_{SCR}).

Although at misorientation angles larger than ~20° the ribbons are close enough to the space charge region edge for the dark and quasi-neutral current density to considerably influence device parameters such as V_{OC} and fill factor (e.g. Fig. 4a,4c), the rapid decrease in total current density with misorientation makes grain textures such as (211) and (221) undesirable for high efficiency devices. A misorientation of 44° for a (221) texture decreases the local efficiency by 3.2% and 3.4% for a passivated and non-passivated symmetric grain boundary respectively, compared to the maximum efficiency of 11.6% for a perfectly oriented Sb₂Se₃ device with no grain boundaries. A similar effect can be seen between the certified efficiency holder of 10.1% [12] consisting of ribbons mainly oriented along the [001] direction, and one of the previous record holders with an efficiency of 7.6% with ribbons having a preferred growth orientation along the (221) plane normal.

Declaration of Competing Interest

The authors declare that they have no known competing financial interests or personal relationships that could have appeared to influence the work reported in this paper.

Acknowledgements

Appendix A. Supplementary data

Supplementary data to this article can be found online at https://doi.org/10.1016/j.solener.2023.112054.

References

[1] Chen, C., Li, W., Zhou, Y., Chen, C., Luo, M., Lio, X., Zeng, K., Yang, B., Zhang, C., Han, J., Tang, J., 2015. Optical properties of amorphous and polycrystalline Sb₂Se₃ thin films prepared by thermal evaporation. Appl. Phys. Lett. 107, 043905. doi: 10.1063/1.4927741.

[2] Tideswell, N.W., Kruse, F.H., McCullough, J.D., 1957. The crystal structure of antimony selenide, Sb₂Se₃. Acta Cryst. 10, 99–102. https://doi.org/10.1107/S0365110X57000298.

[3] Zeng, K., Xue, D.-J., Tang, J., 2016. Antimony selenide thin-film solar cells. Semicond. Sci. Technol. 31 (6), 063001.

[4] McKenna, K.P., 2021. Self-Healing of broken bonds and deep gap states in Sb₂Se₃ and Sb₂S₃. Adv. Electron. Mater. 7, 2000908. https://doi.org/10.1002/aelm.202000908.

[5] Chen, C., Bobela, D.C., Yang, Y., Lu, S., Zeng, K., Ge, C., Yang, B., Gao, L., Zhao, Y., Beard, M.C., Tang, J., 2017. Characterization of basic physical properties of Sb₂Se₃ and its relevance for photovoltaics. Front. Optoelectron. 10, 18–30. https://doi.org/10.1007/s12200-017-0702-z.

[6] Wang, X., Ganose, A.M., Kavanagh, S.R., Walsh, A., 2022. Band versus polaron: charge transport in antimony chalcogenides. ACS Energy Lett. 7, 2954–2960. https://doi.org/10.1021/acsenergylett.2c01464.

[7] Yu, Y., Wang, R.H., Chen, Q., Peng, L.-M., 2006. High-quality ultralong Sb₂Se₃ and Sb₂S₃ nanoribbons on a large scale via a simple chemical route. J. Phys. Chem. B 110 (27), 13415–13419. https://doi.org/10.1021/jp061599d.

[8] Zhou, Y., Wang, L., Chen, S., Qin, S., Liu, X., Chen, J., Xue, D.-J., Luo, M., Cao, Y., Cheng, Y., Sargent, E.H., Tang, J., 2015. Thin-film Sb₂Se₃ photovoltaics with oriented one-dimensional ribbons and benign grain boundaries. Nat. Photonics 9, 409–415. https://doi.org/10.1038/nphoton.2015.78.

[9] Wen, X., Chen, C., Lu, S., Li, K., Kondrotas, R., Zhao, Y., Chen, W., Gao, L., Wang, C., Zhang, J., Niu, G., Tang, J., 2018. Vapor transport deposition of antimony selenide thin film solar cells with 7.6% efficiency. Nat. Commun. 9, 2179. https://doi.org/10.1038/s41467-018-04634-6.

[10] Wang, M., Wang, S., Zhang, Q., Pan, S., Zhao, Y., Zhang, X., 2021. Controlling the crystallographic orientation of Sb₂Se₃ film for efficient photoelectrochemical water splitting. Sol. RRL 6, 2100798. https://doi.org/10.1002/solr.202100798.

[11] Li, Z., Liang, X., Li, G., Liu, H., Zhang, H., Guo, J., Chen, J., Shen, K., San, X., Yu, W., Schropp, R.E.I., Mai, Y., 2019. 9.2%-efficient core-shell structured antimony selenide nanorod array solar cells. Nat. Commun. 10, 125. https://doi.org/10.1038/s41467-018-07903-6.

[12] Duan, Z., Liang, X., Feng, Y., Ma, H., Liang, B., Wang, Y., Luo, S., Wang, S., Schropp, R.E.I., Mai, Y., Li, Z., 2022. Sb₂Se₃ thin-film solar cells exceeding 10% power conversion efficiency enabled by injection vapor deposition technology. Adv. Mater. 34, 2202969. https://doi.org/10.1002/adma.202202969.

[13] Green, M.A., Dunlop, E.D., Yoshita, M., Kopidakis, N., Bothe, K., Siefer, G., Hao, X., 2023. Solar cell efficiency tables (version 62). Prog. Photovolt. Res. Appl. 31, 651-663. doi: 10.1002.pip.3726.

[14] Hutter, O.S., Phillips, L.J., Durose, K., Major, J.D., 2018. 6.6% efficiency antimony selenide solar cells using grain structure control and an organic contact layer. Sol. Energy Mater. Sol. Cells 188, 177–181. https://doi.org/10.1016/j.solmat.2018.09.004.

[15] Synopsys, San Jose, CA, USA, 1986. Technology computer-aided design. https://www.synopsys.com/silicon/tcad.html.

[16] Li, J., Huang, J., Ma, F., Sun, H., Cong, J., Privat, K., Webster, R.F., Cheong, S., Yao, Y., Chin, R.L., Yuan, X., He, M., Sun, K., Li, H., Mai, Y., Hameiri, Z., Ekins-Daukes, N.J., Tilley, R.D., Unold, T., Green, M.A., Hao, X., 2022. Unveiling microscopic carrier loss mechanisms in 12% efficient Cu₂ZnSnSe₄ solar cells. Nat. Energy 7, 754–764. https://doi.org/10.1038/s41560-022-01078-7.

[17] Metzger, W.K., Grover, S., Lu, D., Colegrove, E., Moseley, J., Perkins, C.L., Ki, X., Mallick, R., Zhang, W., Malik, R., Kephart, J., Jiang, C.-S., Kuciauskas, D., Albin, D. S., Al-Jassim, M.M., Xiong, G., Gloeckler, M., 2019. Exceeding 20% efficiency with in situ group V doping in polycrystalline CdTe solar cells. Nat. Energy 4, 837–845. https://doi.org/10.1038/s41560-019-0446-7.

[18] Al Ahmed, S.R., Sunny, A., Rahman, S., 2021. Performance enhancement of Sb2Se3 solar cell using a back surface field layer: a numerical simulation approach. Sol. Energy Mater. Sol. Cells 221, 110919 (13 pages). doi: 10.1016/j.solmat.2020.110919.

[19] Li, Z.Q., Ni, M., Feng, X.D., 2020. Simulation of the Sb₂Se₃ solar cell with a hole transport layer. Mater. Res. Express 7, 016416 (9 pages). doi: 10.1088/2053-1591/ab5fa7.

[20] Sunny, A., Al Ahmed, S.R., 2021. Numerical simulation and performance evaluation of highly efficient Sb₂Se₃ solar cell with tin sulfide as hole transport layer. Phys. Status Solidi B 258, 2000630 (14 pages). doi: 10.1002/pssb.202000630.

[21] Mamta, Maurya, K.K., Singh, V.N., 2021. Sb₂Se₃ versus Sb₂S₃ solar cell: a numerical simulation. Sol. Energy 228, 540-549. doi: 10.1016/j.solener.2021.09.080.

[22] Shaker, A., Salem, M.S., Jayan, K.D., 2022. Analysis and design of p-n homojunction Sb₂Se₃ solar cells by numerical simulation. Sol. Energy 242, 276–286. https://doi.org/10.1016/j.solener.2022.07.035.

[23] Green, M.A., 1982. Solar cells: operating principles, technology, and system applications. Prentice-Hall, United States.

[24] Nelson, J., 2003. The Physics of Solar Cells. Imperial College Press. London, United Kingdom. doi: 10.1142/p276.

[25] Stewart, J., 2016. Calculus, Eight Edition. Cengage Learning. Massachusetts, United States.

[26] Gueymard, C.A., Myers, D., Emergy, K., 2002. Proposed reference irradiance spectra for solar energy system testing. Sol. Energy 73 (6), 443–467. https://doi.org/10.1016/S0038-092X(03)00005-7.

[27] Von Rottkay, K., Rubin, M., 1996. Optical indices of pyrolytic tin-oxide glass. Mater. Res. Soc. Symp. Proc. 426, 449. https://doi.org/10.1557/PROC-426-449.

[28] Jolivet, A., Labbe, C., Frilay, C., Debieu, O., Marie, P., Horcholle, B., Lemarie, F., Portier, X., Grygiel, C., Duprey, S., Jadwisienczak, W., Ingram, D., Upadhyay, M., David, A., Fouchet, A., Luders, U., Cardin, J., 2023. Structural, optical, and electrical properties of TiO₂ thin films deposited by ALD: impact of the substrate, the deposited thickness and deposition temperature. Appl. Surf. Sci. 608, 155214 https://doi.org/10.1016/j.apsusc.2022.155214.

[29] Williams, R., Ramasse, Q., McKenna, K., Phillips, L., Yates, P., Hutter, O., Durose, K., Major, J., Mendis, B., 2020. Evidence for self-healing benign grain boundaries and a highly defective Sb₂Se₃-CdS interfacial layer in Sb₂Se₃ thin-film photovoltaics. ACS Appl. Mater. Interfaces 12, 21730–21738. https://doi.org/10.1021/acsami.0c03690.

[30] Janczarek, M., Kowalska, E., 2017. On the origin of enhanced photocatalytic activity of copper-modified titania in the oxidative reaction systems. Catalysts 7 (11), 317. https://doi.org/10.3390/catal7110317.

[31] Li, Z.-Q., Ni, M., Feng, X.-D., 2020. Simulation of the Sb₂Se₃ solar cell with a hole transport layer. Mater. Res. Express 7 (1), 016416.

[32] Sawicka-Chudy, P., Sibinski, M., Wisz, G., Rybak-Wilusz, E., Cholewa, M., 2018. Numerical analysis and optimization of Cu_2O/TiO_2, CuO/TiO_2, heterojunction solar cells using SCAPS. J. Phys. Conf. Ser. 1033, 012002 https://doi.org/10.1088/1742-6596/1033/1/012002.

[33] Mamta, Maurya, K. K., Singh, V. N., 2021. Efficient Sb_2Se_3 solar cell with higher fill factor: a theoretical approach based on thickness and temperature. Solar Energy 230, 803-809. doi: 10.1016/j.solener.2021.11.002.

[34] Pochont, N.R., Sekhar, Y.R., 2023. Numerical simulation of nitrogen-doped titanium dioxide as an inorganic hole transport layer in mixed halide perovskite structures using SCAPS 1-D. Inorganics 11 (1), 3. https://doi.org/10.3390/inorganics11010003.

[35] Mouchou, R.T., Jen, T.C., Laseinde, O.T., Ukoba, K.O., 2021. Numerical simulation and optimization of p-NiO/n- TiO_2 solar cell system using SCAPS. Mater. Today:. Proc. 38, 835–841. https://doi.org/10.1016/j.matpr.2020.04.880.

[36] Mamta, Maurya, K.K., Singh, V.N., 2022. Sb_2Se_3 as an HTL for Mo/ Sb_2Se_3/ Cs_2TiF_6/ TiO_2 solar structure: performance evaluation with SCAPS-1D. Heliyon 8 (10), e10925.

[37] Kondrotas, R., Chen, C., Tang, J., 2018. Sb_2Se_3 solar cells. Joule 2 (5), 857–878. https://doi.org/10.1016/j.joule.2018.04.003.